Enhanced Oxygen Reduction Performance on {101} $CoMn_2O_4$ Spinel Facets

Ming Zhou,[†,§] Dasol Yoon,[‖,‡,§] Yao Yang,[⊥,§] Lihua Zhang,[▽] Can Li,[†] Hongsen Wang,[⊥] Anju Sharma,[#] Shaojie Jiang,[†] David A. Muller,*[,‖] Héctor D. Abruña,*[,⊥] and Jiye Fang*[,†]

[†]Department of Chemistry, State University of New York at Binghamton, Binghamton, New York 13902, United States.

[‖]School of Applied and Engineering Physics, Cornell University, Ithaca, New York 14853, United States.

[‡]Department of Materials Science and Engineering, Cornell University, Ithaca, New York 14853, United States.

[⊥]Department of Chemistry and Chemical Biology, Cornell University, Ithaca, New York 14853, United States.

[▽]Center for Functional Nanomaterials, Brookhaven National Laboratory, Upton, New York 11973, United States.

[#]Analytical and Diagnostics Lab, State University of New York at Binghamton, Binghamton, New York 13902, United States.

*Corresponding authors:

D.M. david.a.muller@cornell.edu (orcid.org/0000-0003-4129-0473);

H.A. hda1@cornell.edu (orcid.org/0000-0002-3948-356X);

J.F. jfang@binghamton.edu (orcid.org/0000-0003-3703-3204)

[§] These authors contributed equally to this work.

Abstract:

We present a facile colloidal synthesis method to produce uniform-sized (9 nm) $CoMn_2O_4$ spinel nano-octahedra tailored with {101} facets. These nano-octahedra demonstrate enhanced electrocatalytic activity for the oxygen reduction reaction (ORR) in alkaline media compared to their spherical counterparts and previously reported spinel electrocatalysts. At 0.85 V, they achieve a high mass activity (MA) of 60.0 A/g, surpassing the spherical counterparts (38.6 A/g). Moreover, the $CoMn_2O_4$ nano-octahedra exhibit favorable stability, maintaining an MA of 47.2 A/g after 10,000 durability cycles. This work highlights a promising approach for synthesizing advanced spinel nano-oxides with controlled crystal facets, which holds the potential to serve as non-precious metal ORR electrocatalysts. The enhanced ORR performance is attributed to the exposed active catalyst surfaces in the well-defined structures of the nano-octahedra, emphasizing the significance of catalyst shape control.

Hydrogen fuel cells are gaining attention as a renewable energy technology to address global energy demand and environmental pollution caused by fossil fuels.[1-5] However, the sluggish oxygen reduction reaction (ORR) at the cathode,[6-7] the high cost and scarcity of precious metal-based electrocatalysts hinder their widespread industrial use.[8-10] Non-precious metal alkaline ORR electrocatalysts, particularly spinel oxides, offer a low-cost alternative with promising catalytic performance.[11-15] The spinel phase of $Co_xMn_{3-x}O_4$ ($0 < x < 2$) has been reported to exhibit several advantages over other phases for ORR.[16] These advantages include a higher number of catalytic sites on the surface, stronger binding ability to O_2, and a higher average oxidation state of Mn ions with a mixture of Mn^{3+} and Mn^{4+}. This higher oxidation state contributes to enhanced electronic conductivity by facilitating the electron hopping mechanism and improving charge transfer through redox reactions. Recent studies[16-25] have highlighted the importance of surface structures in determining catalytic performance, emphasizing the necessity for spinel oxides with controlled crystal facets. However, the challenging task of identifying the most promising surface of spinel oxides and achieving exclusive facets with the desired ORR performance still persists.

Traditional solid-state approaches yield spinel oxides with irregular morphologies and large particles, limiting their catalytic performance.[26-28] Alternative solution-based methods have been explored,[29-34] but synthesizing ultra-small, monodisperse, crystallographically tailored, and highly efficient spinel oxides for alkaline ORR is highly desirable yet challenging. In this study, we present a facile colloidal synthesis method to produce $CoMn_2O_4$ spinel nano-octahedra with exclusively exposed {101} facets. These nano-octahedra exhibit superior electrocatalytic activity and stability compared to their spherical counterparts and previously reported spinel electrocatalysts (Table S1). To our knowledge, shape-controlled and ultra-small spinel electrocatalysts with such high activity have not been reported before.

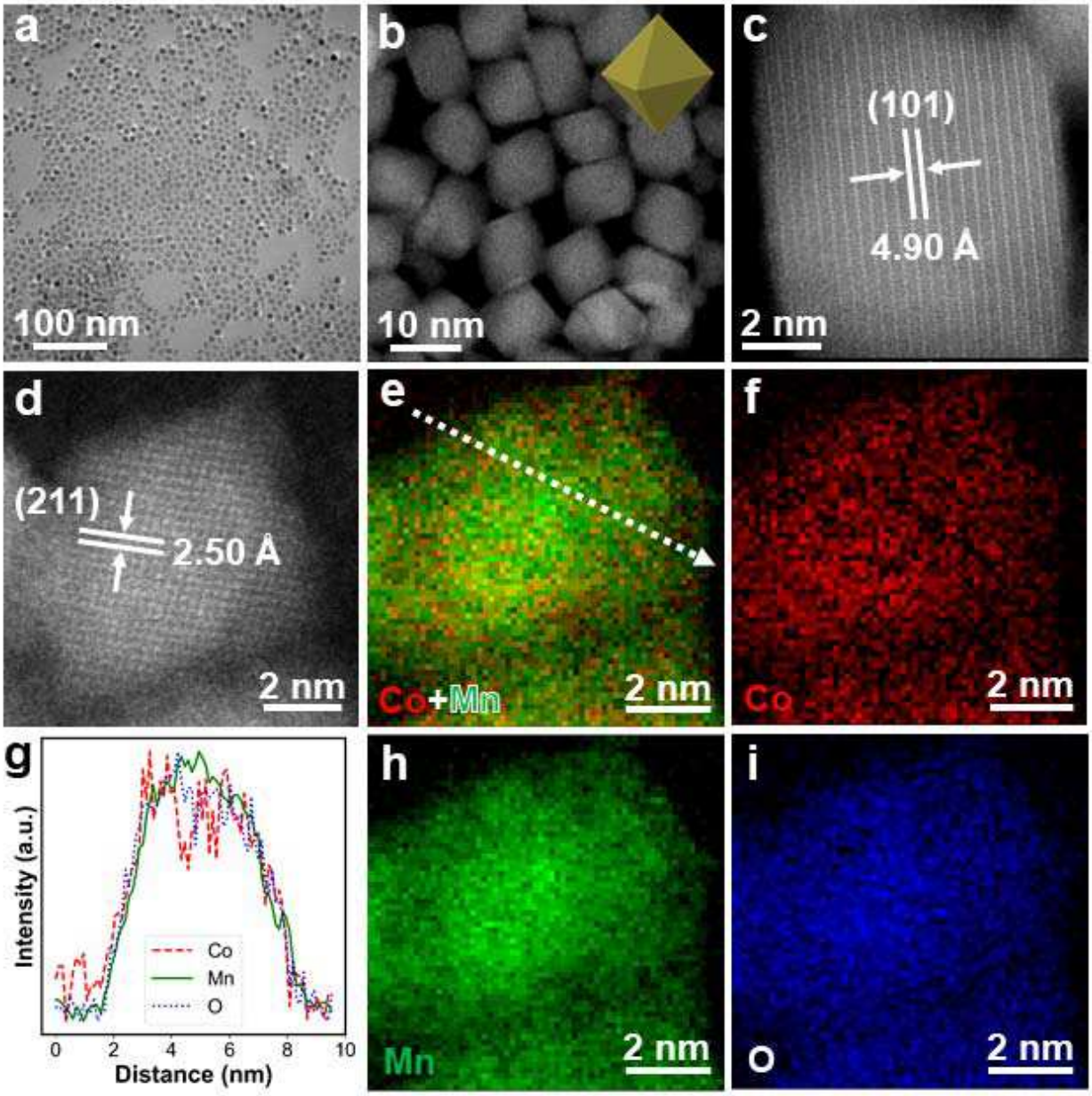

Figure 1. (a) Low-magnification TEM and (b) HAADF-STEM image of the as-prepared $CoMn_2O_4$ nano-octahedra. (c, d) HAADF-STEM images of a representative, as-prepared $CoMn_2O_4$ nano-octahedron. (e, f, h, i) EELS maps of an individual $CoMn_2O_4$ nano-octahedron shown in (d). (g) normalized EELS line scans along the dashed path shown in (e), indicating a homogenous elemental distribution. The inset in (b) displays the 3D model of the octahedral nanocrystal corresponding to the STEM image.

$CoMn_2O_4$ nano-octahedra and nanospheres were synthesized with deliberate control by introducing different types of Co-precursors into the organic reaction solution, followed by an

injection of water at 90 ºC. The details (Figure S1) can be referred to in the Supporting Information. As shown by the low-magnification transmission electron microscopy (TEM) and high-angle annular dark-field scanning transmission electron microscopy (HAADF-STEM) images in Figure 1a-b, at a synthesis time of 24 hours, $CoMn_2O_4$ nanocrystals exhibit a uniformly octahedral morphology enclosed by {101} facets and narrow size distribution with an average edge length of 9.0 ± 0.5 nm (Figure S2a-b). HAADF-STEM images of an individual octahedron are shown in Figure 1c-d, where the lattice spacings were measured to be 4.90 Å and 2.50 Å, respectively, corresponding to the (101) and (211) planes of the $CoMn_2O_4$. The presence of (101) lattice plane was also observed in the high-resolution TEM (HRTEM) image (Figure S2c). The corresponding selected area electron diffraction (SAED) pattern further supports the crystallization of the $CoMn_2O_4$ nano-octahedra in the tetragonal phase of $I4_1/amd$ symmetry (Figure S2d). This observation is consistent with the powder X-ray diffraction (XRD) pattern, as shown in Figure 2a. Moreover, electron energy loss spectroscopy (EELS) elemental maps (Figure 1e, 1f, 1h, and 1i) and normalized line profiles (Figure 1g) were used to investigate the microstructure of $CoMn_2O_4$ nano-octahedra, exhibiting homogenous elemental distributions of Co and Mn. The Co/Mn atomic ratio in $CoMn_2O_4$ nano-octahedra was determined to be 1:1.97 by inductively coupled plasma-optical emission spectroscopy (ICP-OES).

It is well-known that the synthesis of $CoMn_2O_4$ comprises the formation of hydroxides, subsequent oxidation of partial hydroxides into oxyhydroxides, and dissolution-crystallization process to minimize standard Gibbs free energy.[35] It has also been reported that the development of {101}-facet terminated octahedral $CoMn_2O_4$ is highly dependent on the dissolution-crystallization process.[34] In this study, we examined the surface lattice of the as-synthesized

$CoMn_2O_4$ nano-octahedra and determined that they possess {101} facets through analysis of their HAADF-STEM image (Figure S3). Furthermore, we investigated the HRTEM image of a carbon-supported $CoMn_2O_4$ nano-octahedron following accelerated durability tests (ADTs) and verified that the crystal facets remained unchanged (*vide infra*). The key to the successful formation of 9 nm $CoMn_2O_4$ nano-octahedra relies on the use of $CoCl_2 \cdot 6H_2O$, the deliberately selected Co-precursors, with striking discrepancies in reaction kinetics during the dissolution-crystallization process while oleylamine (OAm) provides an alkalescent environment for the synthesis and oleic acid (OA) regulates the alkalinity of the reaction solution. As an example, a replacement of the $CoCl_2 \cdot 6H_2O$ precursors with $Co(acac)_2$, while other synthetic conditions were kept the same, changed the morphology of the resultant $CoMn_2O_4$ to nanospheres. As shown in the low-magnification TEM image, such a replacement results in nearly 100% of spherical $CoMn_2O_4$ nanocrystals (Figure S4a) with an average size of 5.0 ± 0.1 nm (Figure S4b). In the HRTEM images, the spherical nanocrystals exhibit single-crystal spinel structures with good crystallinity (Figure S4c-d). Specifically, the clear lattice fringes with spacings of 2.50 Å and 2.04 Å correspond to lattice planes of (211) and (220) in tetragonal $CoMn_2O_4$, respectively. This observation further reveals that the as-synthesized $CoMn_2O_4$ nanospheres also possess the tetragonal phase. Moreover, the ICP-OES analysis suggests that the Co/Mn atomic ratio of the $CoMn_2O_4$ nanospheres is 1:2.00, almost the same as the nominal composition in the $CoMn_2O_4$ nano-octahedra.

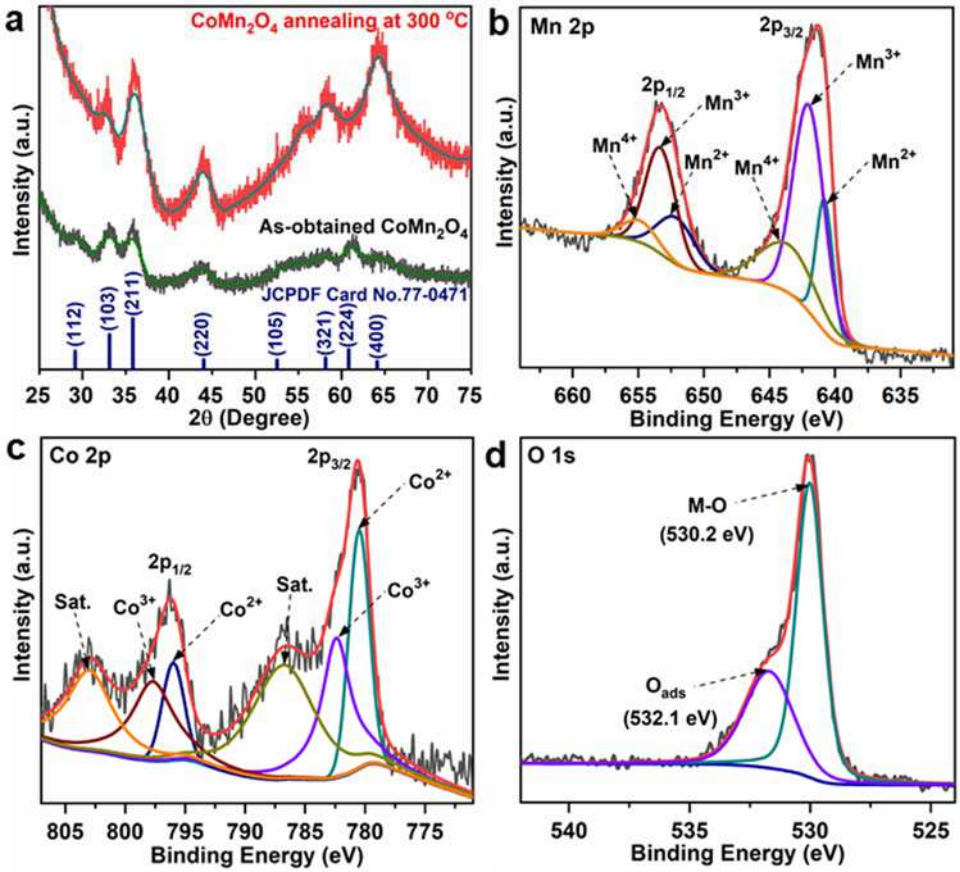

Figure 2. (a) XRD patterns of carbon-supported $CoMn_2O_4$ nano-octahedra before and after annealing. (b-d) XPS spectra of Mn *2p* (b), Co *2p* (c), and O *1s* (d) for carbon-supported $CoMn_2O_4$ nano-octahedra after annealing. Relative ratios of element states: $Mn^{2+}/Mn^{3+}/Mn^{4+}$ = 15/78/7; Co^{2+}/Co^{3+} = 71:29.

Typically, samples synthesized at a low temperature could result in a low crystallinity and abundant ionic deficiency, which can be improved by an annealing treatment. More importantly, thermal treatment in air has been demonstrated as an effective approach for removing surfactants from the nanocrystal surfaces, increasing average metal-oxygen bond length and lowering the average Mn valence in the product.[36-37] We accordingly annealed the carbon-supported $CoMn_2O_4$ nano-octahedra in air at 300 °C for 12 hours, and their crystal phases were further confirmed by XRD. As shown in Figure 2a, all of the detectable peaks in the XRD patterns of the $CoMn_2O_4$ nano-octahedra before and after this thermal treatment match with the standard diffraction lines of

spinel $CoMn_2O_4$ very well (tetragonal, $I4_1/amd$, JCPDS no. 77-0471). The top pattern presented in Figure 2a shows that no phase transition took place for the $CoMn_2O_4$ nano-octahedra during the annealing. Broad peaks determined in both patterns indicate the small sizes of nanocrystallites both before and after this annealing process according to the Scherrer equation.[38-39] Pawley fitting verified the single phase of the octahedral sample both before and after the annealing with an $I4_1/amd$ (141) symmetry as shown in Figure S5. The fitting also indicates that this thermal treatment caused a tiny decrease in cell parameter *a* (from ~5.79 Å to ~5.77 Å) and a slight increase in *c* (from ~9.07 Å to ~9.13 Å), but these changes are insignificant. Furthermore, the valence states of Mn, Co, and O in the $CoMn_2O_4$ nano-octahedra after annealing were investigated using X-ray photoelectron spectroscopy (XPS). The XPS survey spectrum (Figure S6) indicates the coexistence of Co, Mn, and O, in which the atomic ratio of Co to Mn on the surface of the nanocrystals was determined to be 1:2.46. For the Mn *2p* spectrum shown in Figure 2b, the peaks located at 641.0 and 652.3 eV in $CoMn_2O_4$ nano-octahedra are assigned to the Mn^{2+} with a separation of 11.3 eV,[40-42] further demonstrating the successful formation of tetragonal $CoMn_2O_4$ spinel nanocrystals. Meanwhile, the peaks located at 642.2 and 653.5 eV are assigned to the Mn^{3+}, while the others located at 643.8 and 654.8 eV are attributed to Mn^{4+}. XPS analysis suggests that Mn^{2+}, $Mn^{3+,}$ and Mn^{4+} co-existed on the surface of the $CoMn_2O_4$ nano-octahedra with atomic fractions of 15%, 78%, and 7%, respectively, indicating that Mn^{3+} was dominant on the $CoMn_2O_4$ nano-octahedral surface. Similarly, the Co *2p* spectrum (Figure 2c) was also best fitted into two spin-orbit doublets characteristic of Co^{2+} and Co^{3+} and two shake-up satellites (denoted as sat.) using a Gaussian fitting method. The peaks located at 780.7 and 796.0 eV are assigned to the Co^{2+} with a separation of 15.3 eV, while the others located at 782.3 and 797.7 eV are ascribed to Co^{3+}. This result suggests the co-existence of Co^{2+} and Co^{3+} on the surface of the $CoMn_2O_4$ nano-

octahedra comprises molar contributions of 71% and 29%, respectively. Moreover, the oxygen species on the surface of the $CoMn_2O_4$ nano-octahedra were determined from the deconvolution of the O *1s* spectrum in Figure 2d. The peak at 530.2 eV is attributed to the lattice oxygen, while the peak at 532.1 eV is ascribed to the oxygen-containing species absorbed on the surface. The co-existence of $Mn^{2+}/Mn^{3+}/Mn^{4+}$ and Co^{2+}/Co^{3+} in $CoMn_2O_4$ spinels, based on the XPS analysis, is consistent with our previous *Operando* X-ray absorption spectroscopy measurements in which similar Co-Mn spinels, without the shape control, showed synergistic effects between Co and Mn as co-active sites to catalyze the ORR.[12, 43-44] In summary, these results suggest that the surface of the $CoMn_2O_4$ nano-octahedra was predominated by Mn^{3+} and Co^{2+} with an Mn/Co ratio of 2.46:1, further corroborating the formation of the $CoMn_2O_4$ spinel nanocrystals.

To acquire additional insights into the formation mechanism of the $CoMn_2O_4$ spinel nanocrystals, sets of control experiments were conducted. In this case, OAm plays a crucial role as an alkalescent medium during the synthesis. When the synthesis was conducted with the addition of OA in the absence of OAm, no products were generated and only a transparent solution was observed. On the other hand, when only OAm was used as the solvent in the absence of OA, nanoparticles with a relatively broad size distribution were obtained without octahedral products (Figure S7a). Therefore, achieving an appropriate volume ratio of OAm to OA in the synthesis is crucial for controlling the morphology of the final product. Additionally, we found that the selection of Co precursors is critical for the successful formation of octahedral nanocrystals. As previously reported, anions can have a significant impact on the reaction kinetics and thus the morphology of the final product. This is due to the substantial differences in coordination ability between anions and metallic cations.[8, 45] For instance, when $CoBr_2$ was used as the Co precursor,

the majority of the final products appeared as concave nanocubes.[46] This is because Br-ions have a stronger coordination ability with metallic cations and a stronger capping effect on {001} facets (Figure S7b),[8] when compared to Cl-ions and acetylacetone ligands. Furthermore, reducing the volume of water by half resulted in more spherical nanocrystals compared to the octahedral ones (Figure S7c). Based on these observations, it can be inferred that the introduction of water at an elevated temperature may promote the formation of the bimetallic Co-Mn hydroxides as nuclei during the initial reaction stage and prevent the formation of the metal-oleylamine complex. Consequently, we conclude that all the aforementioned factors, including achieving a suitable ratio between OAm and OA, utilizing the appropriate Co precursors, and adjusting the water fraction, play significant roles in determing the formation of $CoMn_2O_4$ octahedral nanocrystals.

To demonstrate a proof-of-concept application, we comparatively evaluated the ORR activities of $CoMn_2O_4$ nano-octahedra and nanospheres that were loaded on carbon and annealed in air at 300 ºC for 12 hours. The rotating disk electrode (RDE) measurement was conducted in 1 M O_2-saturated KOH at 1,600 rpm for this purpose. Figure 3a shows that the ORR polarization profile of the benchmark Pt/C exhibited a half-wave potential ($E_{1/2}$) of 0.890 V *vs.* reversible hydrogen electrode (RHE), which is considered a benchmark activity value in O_2-saturated 1 M KOH at a scan rate of 5 mV/s and a rotation rate of 1,600 rpm. It is worth noting that 1 M KOH is more similar to the realistic OH^- concentration in practical membrane electrode assembly (MEA) tests, as opposed to 0.1 M KOH.[47-48] The ORR polarization profiles of both the $CoMn_2O_4$ sample and benchmark Pt/C showed similar diffusion-limited current density, i_d, of approximately −3.7 mA/cm^2, indicating a leading role of the 4e$^-$ process in reducing O_2 to H_2O based on the Levich equation,[49] instead of the 2e$^-$ process of forming peroxide species. Moreover, the $CoMn_2O_4$ nano-

octahedra exhibited a more positive $E_{1/2}$ value of 0.875 V *vs.* RHE, which is 25 mV higher than that of $CoMn_2O_4$ nanospheres (0.85 V), revealing that the $CoMn_2O_4$ nano-octahedra have better alkaline ORR catalytic activity than the nanospheres. Unlike Pt or other transition metal electrocatalysts, for which the electrochemical active surface area (ECSA) can be typically determined using hydrogen underpotential deposition (H_{UPD}) or CO-stripping methods, it is quite challenging to accurately evaluate the ECSA of oxide electrocatalysts although several methods have been under development.[50-52] As exemplified in the recent literature,[12, 43-44, 53-54] in this work we only focus on the mass activity-based assessment due to the lack of a benchmark ECSA measurement approach for spinels. To quantitatively evaluate the activity of the $CoMn_2O_4$ nano-octahedra and nanospheres, we calculated the mass activity (MA) at 0.85 V by normalizing the kinetic current to the mass loading of metal oxides. As depicted in Figure 3b, the MA at 0.85 V of the $CoMn_2O_4$ nano-octahedra, with a value of 60.0 A/g, was approximately 1.6 times and ~1.9 times as high as the values measured for $CoMn_2O_4$ nanospheres in this study (38.6 A/g) and reported earlier (31 A/g),[12] respectively. The superior ORR activity of the $CoMn_2O_4$ nano-octahedra was further supported by the smaller Tafel slope of 42.1 mV/decade compared to those measured from the $CoMn_2O_4$ nanospheres (46.3 mV/decade) and the benchmark Pt/C (61.6 mV/decade), indicating a lower overpotential required to achieve the same kinetic current change (Figure S8). As a result, the enhanced alkaline ORR activity of $CoMn_2O_4$ nano-octahedra compared to $CoMn_2O_4$ nanospheres is likely attributed to the {101} planes exclusively exposed on the catalyst surface. The ORR kinetics of the $CoMn_2O_4$ nano-octahedra in 1 M KOH were subsequently investigated using RDE measurements at different rotation rates. Figure 3c-d shows the ORR polarization profiles of the $CoMn_2O_4$ nano-octahedra in O_2-saturated 1 M KOH at a scan rate of 5 mV/s at the different rotation rates and the corresponding Koutecky-Levich plots at

different potentials, respectively. According to the slopes of Koutecky–Levich plots, the electron transfer number (n) can be determined with a value of ~3.9 at 0.60-0.75 V, further revealing a $4e^-$ oxygen reduction process on $CoMn_2O_4$ nano-octahedra, similar to the case of the benchmark Pt/C.[5]

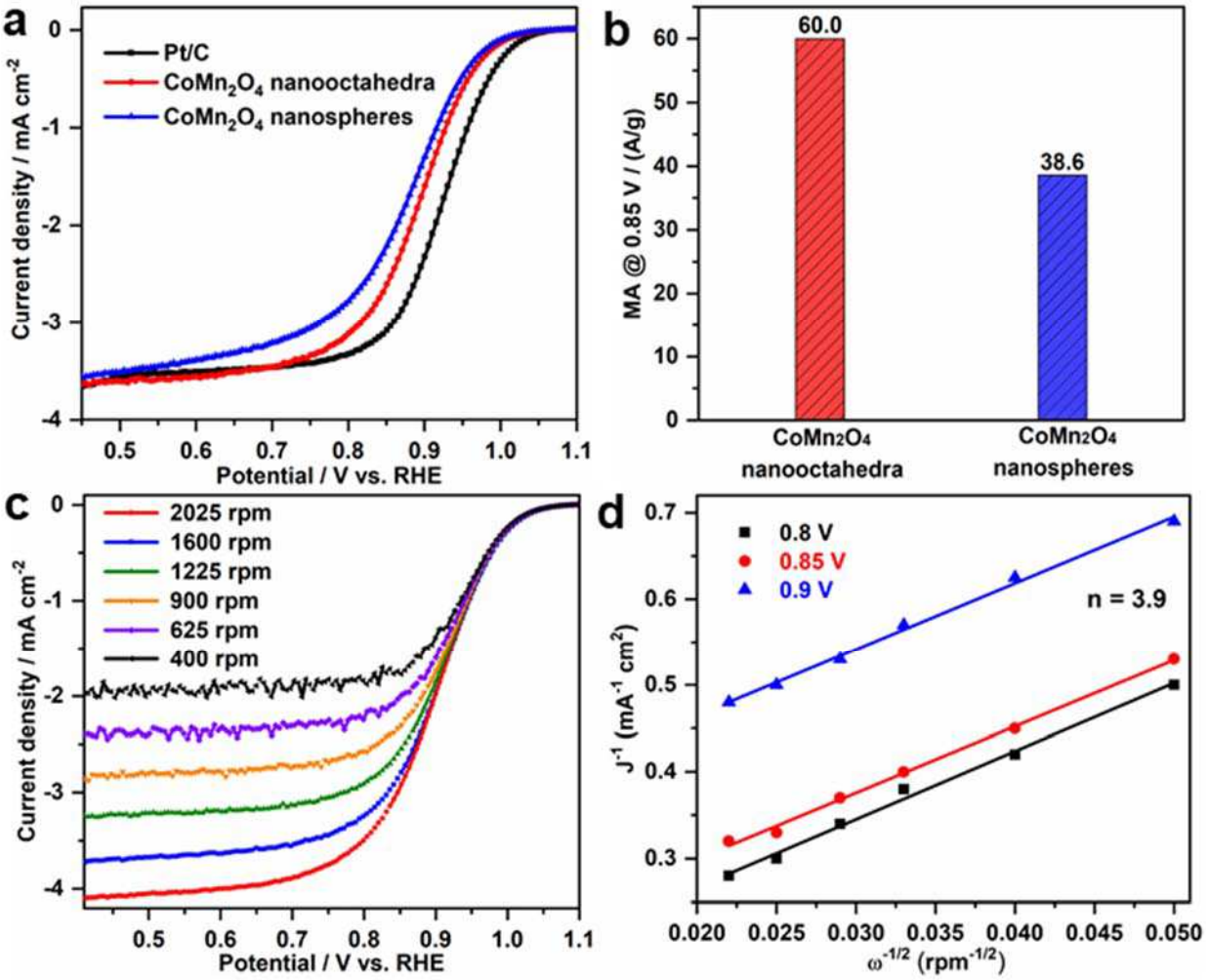

Figure 3. (a) ORR polarization profiles of $CoMn_2O_4$ nano-octahedra, $CoMn_2O_4$ nanospheres and benchmark Pt/C, in O_2-saturated 1 M KOH at a scan rate of 5 mV/s at 1,600 rpm. (b) Mass activities of $CoMn_2O_4$ nano-octahedra and $CoMn_2O_4$ nanospheres at 0.85 V *vs.* RHE, which was calculated by normalizing the kinetic current to the mass loading of metal oxide. (c) $CoMn_2O_4$ nano-octahedra in O_2-saturated 1 M KOH at a scan rate of 5 mV/s at the different rotation rates indicated. (d) Corresponding Koutecky-Levich plots (J^{-1} *vs.* $\omega^{-1/2}$) at different potentials. The electron transfer number (n) was calculated to be ~3.9 at 0.85 V based on the slopes of Koutecky-Levich plots. Spinel samples were annealed in air at 300 °C for 12 hours before these measurements.

The $CoMn_2O_4$ nano-octahedral catalyst also exhibited remarkable durability in addition to its significant enhancement in MA, outperforming both the $CoMn_2O_4$ nanospheres and the benchmark Pt/C. After 10,000 cycles of ADTs at room temperature with potential cycling between 0.6 to 1.0 V at 100 mV/s, the $CoMn_2O_4$ nano-octahedral catalyst showed an activity decay with a $\Delta E_{1/2}$ value of 24 mV, which is superior to the benchmark Pt/C with a $\Delta E_{1/2}$ value of 28 mV (Figure 4). Specifically, the MA at 0.85 V only dropped to 47.2 A/g, representing a loss of 21% relative to the pristine MA. Nevertheless, this value was still 22% higher than the MA of the pristine $CoMn_2O_4$ nano-spherical catalyst, indicating the promising stability of the $CoMn_2O_4$ nano-octahedra. The activity decay was found to be caused by a gradual decrease in the ECSA due to particle aggregation/sintering during long-term potential cycles, as shown by the cyclic voltammetric (CV) measurements before and after the ADTs (Figure S9). However, low-magnification (Figure S10a) and high-magnification (Figure S10b) of the HAADF-STEM images and HRTEM image (Figure S10c) of the carbon-supported $CoMn_2O_4$ nano-octahedra revealed that the size, morphology, and crystal phase were still well-preserved after the ADTs. The diffractogram (the inset in Figure S10c) obtained from a fast Fourier transform (FFT) on the basis of Figure S10c and structural models in different zone axes (Figure S10d,e) further indicate the unchanged {101} crystal facets after the ADTs. Furthermore, STEM-EDX mapping (Figure S10f-h) and corresponding EDX line scan (Figure S11) confirmed the octahedral morphology of $CoMn_2O_4$ nano-octahedra and the uniform distribution of compositions Mn and Co elements after the ADTs, with Mn/Co ratio of 1.92 :1. Additionally, XPS analysis was carried out to determine the chemical valence states of Mn and Co after the ADTs. The results show that $Mn^{2+}/Mn^{3+}/Mn^{4+}$ = 23:62:15 and Co^{2+}/Co^{3+} = 70:30. The fraction of Mn^{3+} in Mn element, indicated by $Mn^{3+}/(Mn^{2+} + Mn^{3+} + Mn^{4+})$, decreased from 78% (before the ADTs) to 62% (after the ADTs, Figure S12a). Meanwhile, the ratio of Co^{2+} to Co^{3+}

remained relatively unchanged before (Co^{2+}/Co^{3+} = 71:29) and after the ADTs (Co^{2+}/Co^{3+} = 70:30, Figure S12b) the ADTs. This finding is consistent with a previous study that showed a strong correlation between the ORR activity and the valent states of Mn on the surface of Mn-based spinel oxides.[14] This suggests that the decrease in the relative amount of Mn^{3+} contents on the surface of $CoMn_2O_4$ nano-octahedra may be responsible for the decrease in ORR activity, as Mn ions have been identified as the key active sites for O_2 activation, while Co serves as the co-catalytic sites for the activation of interfacial water.[55] In addition, noticeable surface area decay was observed in CV profiles after 10,000 potential cycles, indicating a mild particle aggregation (Figures S9a and S10a). Taken together, these results demonstrate the promising catalytic durability of the octahedral nanocrystals synthesized in the reported approach.

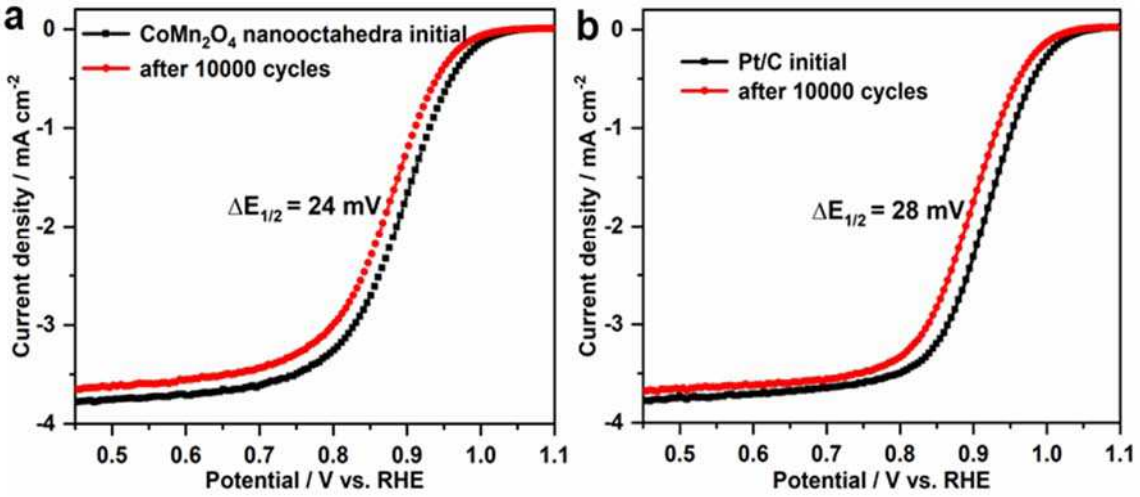

Figure 4. ORR polarization profiles of (a) $CoMn_2O_4$ nano-octahedra (annealed in air at 300 °C for 12 hours) and (b) Pt/C at a scan rate of 5 mV/s at 1,600 rpm. The accelerated durability tests were performed in O_2-saturated 1 M KOH at a scan rate of 100 mV/s from 0.6 to 1.0 V *vs.* RHE.

This study presents a simple and efficient method for synthesizing uniform $CoMn_2O_4$ spinel nano-octahedra with exclusively exposed {101} planes. The electrocatalytic evaluation demonstrates that these nano-octahedra outperform their nano-spherical counterparts and previously reported catalysts in terms of activity and stability for ORR in alkaline media. We attribute the decline in ORR activity over time to the decrease in Mn^{3+} content on the octahedral surface of the catalyst. This research not only introduces a novel strategy for producing spinel-based nanocrystals with enhanced ORR performance but also provides valuable insights into the facet-dependent behavior of the ORR. Overall, our findings pave the way for further exploration of facet-engineered catalysts in efficient ORR applications, opening up new avenues for advancements in this field.

Supporting Information

Supporting Information is available.

- (1) Experimental section, (2) Supplemental Table and Figures, including the schematic illustration of sample preparation procedure; TEM images and size distributions of $CoMn_2O_4$ nano-octahedra and nanospheres; HAADF-STEM image and structural model of the as-prepared $CoMn_2O_4$ nano-octahedron; lattice parameter Pawley fitting of carbon-supported $CoMn_2O_4$ nano-octahedra; survey spectrum of annealed $CoMn_2O_4$ nano-octahedra; TEM images of $CoMn_2O_4$ nanocrystals synthesized under different conditions; Tafel plots of $CoMn_2O_4$ nano-octahedra, $CoMn_2O_4$ nanospheres, and Pt/C; CV curves of annealed $CoMn_2O_4$ nano-octahedra and Pt/C at initial and after 10,000 potential cycles; TEM/HAADF-STEM images, structural models, and EDX elemental mappings of $CoMn_2O_4$ nano-octahedron after durability tests; and (3) References.

Acknowledgments

This work was supported as part of the Center for Alkaline Based Energy Solutions (CABES), an Energy Frontier Research Center funded by the U.S. Department of Energy (DOE), Office of Science, Basic Energy Sciences at Binghamton University under award # DE-SC0019445. We also acknowledge the National Science Foundation, under Grant # DMR-1808383, for its partial support to M.Z. and C.L.. Y.Y. and D.Y. acknowledge that the STEM-EELS work made use of

the Cornell Center for Materials Research Shared Facilities which are supported through the NSF MRSEC program (DMR-1719875). L.Z. acknowledges the use of TEM facilities for the structural characterizations, at the Center for Functional Nanomaterials, which is a U.S. DOE Office of Science User Facility, at Brookhaven National Laboratory under Contract No. DE-SC0012704. Partial low-magnification TEM imaging and XPS work was supported by S3IP/ADL, State University of New York at Binghamton. M.Z. thanks Yang Peng and Mingjiu Liu for their help in carrying out some experiments.

Author Contributions

§these authors contributed equally to this work.

Notes

The authors declare no competing financial interest.

References

1. Stamenkovic, V. R.; Strmcnik, D.; Lopes, P. P.; Markovic, N. M. Energy and Fuels from Electrochemical Interfaces. *Nat. Mater.* **2017,** *16* (1), 57-69.

2. Debe, M. K. Electrocatalyst Approaches and Challenges for Automotive Fuel Cells. *Nature* **2012,** *486* (7401), 43-51.

3. Seh, Z. W.; Kibsgaard, J.; Dickens, C. F.; Chorkendorff, I.; Nørskov, J. K.; Jaramillo, T. F. Combining Theory and Experiment in Electrocatalysis: Insights into Materials Design. *Science* **2017,** *355* (6321), eaad4998.

4. Zhang, J.; Yang, H.; Fang, J.; Zou, S. Synthesis and Oxygen Reduction Activity of Shape-Controlled Pt_3Ni Nanopolyhedra. *Nano Lett.* **2010,** *10* (2), 638-644.

5. Liang, Y.; Li, Y.; Wang, H.; Zhou, J.; Wang, J.; Regier, T.; Dai, H. Co_3O_4 Nanocrystals on Graphene as a Synergistic Catalyst for Oxygen Reduction Reaction. *Nat. Mater.* **2011,** *10* (10), 780-786.

6. Choi, S.-I.; Xie, S.; Shao, M.; Odell, J. H.; Lu, N.; Peng, H.-C.; Protsailo, L.; Guerrero, S.; Park, J.; Xia, X.; Wang, J.; Kim, M. J.; Xia, Y. Synthesis and Characterization of 9 nm Pt–Ni Octahedra with a Record High Activity of 3.3 A/mg_{Pt} for the Oxygen Reduction Reaction. *Nano Lett.* **2013,** *13* (7), 3420-3425.

7. Liang, Y.; Wang, H.; Zhou, J.; Li, Y.; Wang, J.; Regier, T.; Dai, H. Covalent Hybrid of Spinel Manganese–Cobalt Oxide and Graphene as Advanced Oxygen Reduction Electrocatalysts. *J. Am. Chem. Soc.* **2012,** *134* (7), 3517-3523.

8. Zhou, M.; Wang, H.; Vara, M.; Hood, Z. D.; Luo, M.; Yang, T.-H.; Bao, S.; Chi, M.; Xiao, P.; Zhang, Y.; Xia, Y. Quantitative Analysis of the Reduction Kinetics Responsible for the One-Pot Synthesis of Pd–Pt Bimetallic Nanocrystals with Different Structures. *J. Am. Chem. Soc.* **2016,** *138* (37), 12263-12270.

9. Rudi, S.; Teschner, D.; Beermann, V.; Hetaba, W.; Gan, L.; Cui, C.; Gliech, M.; Schlögl, R.; Strasser, P. pH-Induced versus Oxygen-Induced Surface Enrichment and Segregation Effects in Pt–Ni Alloy Nanoparticle Fuel Cell Catalysts. *ACS Catal.* **2017,** *7* (9), 6376-6384.

10. Zhang, L.; Fischer, J. M. T. A.; Jia, Y.; Yan, X.; Xu, W.; Wang, X.; Chen, J.; Yang, D.; Liu, H.; Zhuang, L.; Hankel, M.; Searles, D. J.; Huang, K.; Feng, S.; Brown, C. L.; Yao, X. Coordination of Atomic Co–Pt Coupling Species at Carbon Defects as Active Sites for Oxygen Reduction Reaction. *J. Am. Chem. Soc.* **2018,** *140* (34), 10757-10763.

11. Cheng, F.; Shen, J.; Peng, B.; Pan, Y.; Tao, Z.; Chen, J. Rapid Room-Temperature Synthesis of Nanocrystalline Spinels as Oxygen Reduction and Evolution Electrocatalysts. *Nat. Chem.* **2011,** *3* (1), 79-84.

12. Yang, Y.; Xiong, Y.; Holtz, M. E.; Feng, X.; Zeng, R.; Chen, G.; DiSalvo, F. J.; Muller, D. A.; Abruña, H. D. Octahedral Spinel Electrocatalysts for Alkaline Fuel Cells. *Proc. Natl. Acad. Sci.* **2019,** *116* (49), 24425-24432.

13. Zhou, Y.; Sun, S.; Xi, S.; Duan, Y.; Sritharan, T.; Du, Y.; Xu, Z. J. Superexchange Effects on Oxygen Reduction Activity of Edge-Sharing [$Co_xMn_{1-x}O_6$] Octahedra in Spinel Oxide. *Adv. Mater.* **2018,** *30* (11), 1705407.

14. Zhou, Y.; Xi, S.; Wang, J.; Sun, S.; Wei, C.; Feng, Z.; Du, Y.; Xu, Z. J. Revealing the Dominant Chemistry for Oxygen Reduction Reaction on Small Oxide Nanoparticles. *ACS Catal.* **2018,** *8* (1), 673-677.

15. Eom, C. J.; Kuo, D.-Y.; Adamo, C.; Moon, E. J.; May, S. J.; Crumlin, E. J.; Schlom, D. G.; Suntivich, J. Tailoring Manganese Oxide with Atomic Precision to Increase Surface Site Availability for Oxygen Reduction Catalysis. *Nat. Commun.* **2018,** *9* (1), 4034.

16. Li, C.; Han, X.; Cheng, F.; Hu, Y.; Chen, C.; Chen, J. Phase and Composition Controllable Synthesis of Cobalt Manganese Spinel Nanoparticles towards Efficient Oxygen Electrocatalysis. *Nat. Commun.* **2015,** *6* (1), 7345.

17. Lu, F.; Zhang, Y.; Liu, S.; Lu, D.; Su, D.; Liu, M.; Zhang, Y.; Liu, P.; Wang, J. X.; Adzic, R. R.; Gang, O. Surface Proton Transfer Promotes Four-Electron Oxygen Reduction on Gold Nanocrystal Surfaces in Alkaline Solution. *J. Am. Chem. Soc.* **2017,** *139* (21), 7310-7317.

18. Gan, L.; Rudi, S.; Cui, C.; Heggen, M.; Strasser, P. Size-Controlled Synthesis of Sub-10 nm $PtNi_3$ Alloy Nanoparticles and their Unusual Volcano-Shaped Size Effect on ORR Electrocatalysis. *Small* **2016,** *12* (23), 3189-3196.

19. Choi, M.; Siepser, N. P.; Jeong, S.; Wang, Y.; Jagdale, G.; Ye, X.; Baker, L. A. Probing Single-Particle Electrocatalytic Activity at Facet-Controlled Gold Nanocrystals. *Nano Lett.* **2020,** *20* (2), 1233-1239.

20. Liu, J.; Jiang, L.; Zhang, B.; Jin, J.; Su, D. S.; Wang, S.; Sun, G. Controllable Synthesis of Cobalt Monoxide Nanoparticles and the Size-Dependent Activity for Oxygen Reduction Reaction. *ACS Catal.* **2014,** *4* (9), 2998-3001.

21. Meng, Y.; Song, W.; Huang, H.; Ren, Z.; Chen, S.-Y.; Suib, S. L. Structure–Property Relationship of Bifunctional MnO_2 Nanostructures: Highly Efficient, Ultra-Stable Electrochemical Water

Oxidation and Oxygen Reduction Reaction Catalysts Identified in Alkaline Media. *J. Am. Chem. Soc.* **2014,** *136* (32), 11452-11464.

22. Rudel, H. E.; Lane, M. K. M.; Muhich, C. L.; Zimmerman, J. B. Toward Informed Design of Nanomaterials: A Mechanistic Analysis of Structure–Property–Function Relationships for Faceted Nanoscale Metal Oxides. *ACS Nano* **2020,** *14* (12), 16472-16501.

23. Gonell, F.; Sánchez-Sánchez, C. M.; Vivier, V.; Méthivier, C.; Laberty-Robert, C.; Portehault, D. Structure–Activity Relationship in Manganese Perovskite Oxide Nanocrystals from Molten Salts for Efficient Oxygen Reduction Reaction Electrocatalysis. *Chem. Mater.* **2020,** *32* (10), 4241-4247.

24. Jung, J.-I.; Park, S.; Kim, M.-G.; Cho, J. Tunable Internal and Surface Structures of the Bifunctional Oxygen Perovskite Catalysts. *Adv. Energy Mater.* **2015,** *5* (24), 1501560.

25. Suntivich, J.; Gasteiger, H. A.; Yabuuchi, N.; Nakanishi, H.; Goodenough, J. B.; Shao-Horn, Y. Design Principles for Oxygen-Reduction Activity on Perovskite Oxide Catalysts for Fuel Cells and Metal–Air Batteries. *Nat. Chem.* **2011,** *3* (7), 546-550.

26. Armijo, J. S. The Kinetics and Mechanism of Solid-State Spinel Formation — A Review and Critique. *Oxid. Met.* **1969,** *1* (2), 171-198.

27. Zhao, Q.; Yan, Z.; Chen, C.; Chen, J. Spinels: Controlled Preparation, Oxygen Reduction/Evolution Reaction Application, and Beyond. *Chem. Rev.* **2017,** *117* (15), 10121-10211.

28. Zhao, A.; Masa, J.; Xia, W.; Maljusch, A.; Willinger, M.-G.; Clavel, G.; Xie, K.; Schlögl, R.; Schuhmann, W.; Muhler, M. Spinel Mn–Co Oxide in N-Doped Carbon Nanotubes as a Bifunctional Electrocatalyst Synthesized by Oxidative Cutting. *J. Am. Chem. Soc.* **2014,** *136* (21), 7551-7554.

29. Wang, Z.; Huang, J.; Wang, L.; Liu, Y.; Liu, W.; Zhao, S.; Liu, Z.-Q. Cation-Tuning Induced d-Band Center Modulation on Co-Based Spinel Oxide for Oxygen Reduction/Evolution Reaction. *Angew. Chem. Int. Ed.* **2022,** *61* (16), e202114696.

30. Wei, C.; Feng, Z.; Scherer, G. G.; Barber, J.; Shao-Horn, Y.; Xu, Z. J. Cations in Octahedral Sites: A Descriptor for Oxygen Electrocatalysis on Transition-Metal Spinels. *Adv. Mater.* **2017,** *29* (23), 1606800.

31. Sanna Angotzi, M.; Musinu, A.; Mameli, V.; Ardu, A.; Cara, C.; Niznansky, D.; Xin, H. L.; Cannas, C. Spinel Ferrite Core–Shell Nanostructures by a Versatile Solvothermal Seed-Mediated Growth Approach and Study of Their Nanointerfaces. *ACS Nano* **2017,** *11* (8), 7889-7900.

32. Wei, T.-Y.; Chen, C.-H.; Chien, H.-C.; Lu, S.-Y.; Hu, C.-C. A Cost-Effective Supercapacitor Material of Ultrahigh Specific Capacitances: Spinel Nickel Cobaltite Aerogels from an Epoxide-Driven Sol–Gel Process. *Adv. Mater.* **2010,** *22* (3), 347-351.

33. Ching, S.; Welch, E. J.; Hughes, S. M.; Bahadoor, A. B. F.; Suib, S. L. Nonaqueous Sol−Gel Syntheses of Microporous Manganese Oxides. *Chem. Mater.* **2002,** *14* (3), 1292-1299.

34. Yao, L.; Zhang, L.; Liu, Y.; Tian, L.; Xu, J.; Liu, T.; Liu, D.; Wang, C. $MnCo_2O_4$ and $CoMn_2O_4$ Octahedral Nanocrystals Synthesized via a One-Step Co-Precipitation Process and Their Catalytic Properties in Benzyl Alcohol Oxidation. *CrystEngComm* **2016,** *18* (46), 8887-8897.

35. Liu, Y.; Wang, Y.; Xu, X.; Sun, P.; Chen, T. Facile One-Step Room-Temperature Synthesis of Mn-Based Spinel Nanoparticles for Electro-Catalytic Oxygen Reduction. *RSC Adv.* **2014,** *4* (9), 4727-4731.

36. Li, P.; Nan, C.; Wei, Z.; Lu, J.; Peng, Q.; Li, Y. Mn_3O_4 Nanocrystals: Facile Synthesis, Controlled Assembly, and Application. *Chem. Mater.* **2010,** *22* (14), 4232-4236.

37. Godillot, G.; Guerlou-Demourgues, L.; Croguennec, L.; Shaju, K. M.; Delmas, C. Effect of Temperature on Structure and Electronic Properties of Nanometric Spinel-Type Cobalt Oxides. *J. Phys. Chem. C* **2013,** *117* (18), 9065-9075.

38. Klug, H. P.; Alexander, L. E. *X-Ray Diffraction Procedures for Polycrystalline and Amorphous Materials*. 2nd ed.; John Wiley & Sons: New York, 1954; p 687-690.

39. Cullity, B. D. *Elements of X-Ray Diffraction*. 2nd ed.; Addison-Wesley: Reading, 1978; p 101-102.

40. Zhu, H.; Yu, D.; Zhang, S.; Chen, J.; Wu, W.; Wan, M.; Wang, L.; Zhang, M.; Du, M. Morphology and Structure Engineering in Nanofiber Reactor: Tubular Hierarchical Integrated Networks Composed of Dual Phase Octahedral $CoMn_2O_4$/Carbon Nanofibers for Water Oxidation. *Small* **2017,** *13* (26), 1700468.

41. Ge, X.; Liu, Y.; Goh, F. W. T.; Hor, T. S. A.; Zong, Y.; Xiao, P.; Zhang, Z.; Lim, S. H.; Li, B.; Wang, X.; Liu, Z. Dual-Phase Spinel $MnCo_2O_4$ and Spinel $MnCo_2O_4$/Nanocarbon Hybrids for Electrocatalytic Oxygen Reduction and Evolution. *ACS Appl. Mater. Interfaces* **2014,** *6* (15), 12684-12691.

42. Lai, F.; Miao, Y.-E.; Huang, Y.; Chung, T.-S.; Liu, T. Flexible Hybrid Membranes of $NiCo_2O_4$-Doped Carbon Nanofiber@MnO_2 Core–Sheath Nanostructures for High-Performance Supercapacitors. *J. Phys. Chem. C* **2015,** *119* (24), 13442-13450.

43. Yang, Y.; Wang, Y.; Xiong, Y.; Huang, X.; Shen, L.; Huang, R.; Wang, H.; Pastore, J. P.; Yu, S.-H.; Xiao, L.; Brock, J. D.; Zhuang, L.; Abruña, H. D. In Situ X-ray Absorption Spectroscopy of a Synergistic Co–Mn Oxide Catalyst for the Oxygen Reduction Reaction. *J. Am. Chem. Soc.* **2019,** *141* (4), 1463-1466.

44. Xiong, Y.; Yang, Y.; Feng, X.; DiSalvo, F. J.; Abruña, H. D. A Strategy for Increasing the Efficiency of the Oxygen Reduction Reaction in Mn-Doped Cobalt Ferrites. *J. Am. Chem. Soc.* **2019,** *141* (10), 4412-4421.

45. Chen, Q.; Zhang, J.; Jia, Y.; Jiang, Z.; Xie, Z.; Zheng, L. Wet Chemical Synthesis of Intermetallic Pt_3Zn Nanocrystals via Weak Reduction Reaction together with UPD Process and Their Excellent Electrocatalytic Performances. *Nanoscale* **2014,** *6* (12), 7019-7024.

46. Hogan, D. W.; Dyson, D. J. Angles between Planes in the Hexagonal and Tetragonal Crystal Systems. *Micron (1969)* **1970,** *2* (1), 59-61.

47. Peng, H.; Li, Q.; Hu, M.; Xiao, L.; Lu, J.; Zhuang, L. Alkaline Polymer Electrolyte Fuel Cells Stably Working at 80 °C. *J. Power Sources* **2018,** *390*, 165-167.

48. Yang, Y.; Peng, H.; Xiong, Y.; Li, Q.; Lu, J.; Xiao, L.; DiSalvo, F. J.; Zhuang, L.; Abruña, H. D. High-Loading Composition-Tolerant Co–Mn Spinel Oxides with Performance beyond 1 W/cm^2 in Alkaline Polymer Electrolyte Fuel Cells. *ACS Energy Lett.* **2019,** *4* (6), 1251-1257.

49. Davis, R. E.; Horvath, G. L.; Tobias, C. W. The Solubility and Diffusion Coefficient of Oxygen in Potassium Hydroxide Solutions. *Electrochim. Acta* **1967,** *12* (3), 287-297.

50. Zhao, S.; Yu, H.; Maric, R.; Danilovic, N.; Capuano, C. B.; Ayers, K. E.; Mustain, W. E. Calculating the Electrochemically Active Surface Area of Iridium Oxide in Operating Proton Exchange Membrane Electrolyzers. *J. Electrochem. Soc.* **2015,** *162* (12), F1292-F1298.

51. Cossar, E.; Houache, M. S. E.; Zhang, Z.; Baranova, E. A. Comparison of Electrochemical Active Surface Area Methods for Various Nickel Nanostructures. *J. Electroanal. Chem.* **2020,** *870*, 114246.

52. Connor, P.; Schuch, J.; Kaiser, B.; Jaegermann, W. The Determination of Electrochemical Active Surface Area and Specific Capacity Revisited for the System MnO_x as an Oxygen Evolution Catalyst. *Z. Phys. Chem.* **2020,** *234* (5), 979-994.

53. Yang, Y.; Zeng, R.; Xiong, Y.; DiSalvo, F. J.; Abruña, H. D. Cobalt-Based Nitride-Core Oxide-Shell Oxygen Reduction Electrocatalysts. *J. Am. Chem. Soc.* **2019,** *141* (49), 19241-19245.

54. Yousefi, E.; Ghorbani, M.; Dolati, A.; Yashiro, H.; Outokesh, M. Preparation of New Titanium Nitride-Carbon Nanocomposites in Supercritical Benzene and Their Oxygen Reduction Activity in Alkaline Medium. *Electrochim. Acta* **2015,** *164*, 114-124.

55. Wang, Y.; Yang, Y.; Jia, S.; Wang, X.; Lyu, K.; Peng, Y.; Zheng, H.; Wei, X.; Ren, H.; Xiao, L.; Wang, J.; Muller, D. A.; Abruña, H. D.; Hwang, B. J.; Lu, J.; Zhuang, L. Synergistic Mn-Co Catalyst Outperforms Pt on High-Rate Oxygen Reduction for Alkaline Polymer Electrolyte Fuel Cells. *Nat. Commun.* **2019,** *10* (1), 1506.

TOC Graphic